A novel method to detect the tropopause structure based on bi-Gaussian function

Kun Zhang[1,2,3], Tao Luo[1,2,3], Xuebin Li[1,2,3], Shengcheng Cui[2,3], Ningquan Weng[2,3], Yinbo Huang[2,3], Yingjian Wang[1,2,3]

[1]State Key Laboratory of Laser Interaction with Matter, Anhui Institute of Optics and Fine Mechanics, HFIPS, Chinese Academy of Sciences, Hefei, 230031, China
[2]Key Laboratory of Atmospheric Optics, Anhui Institute of Optics and Fine Mechanics, Hefei Institutes of Physical Science, Chinese Academy of Sciences, Hefei, 230031, China
[3]Advanced Laser Technology Laboratory of Anhui Province, Hefei, 230037, China

Correspondence to: Tao Luo (luotao@aiofm.ac.cn); Xuebin Li (xbli@aiofm.ac.cn)

Abstract. The tropopause is an important transition layer, and can be a diagnostic of the upper troposphere and lower stratosphere structures, with unique atmospheric thermal and dynamic structures. A comprehensive understanding of the evolution of the fine tropopause structures is necessary and primary to further study the complex multi-scale atmospheric physical–chemical coupling processes in the upper troposphere and lower stratosphere. Utilizing the bi-Gaussian function, a novel method is capable of identifying the characteristic parameters of tropopause vertical structures, as well as providing the information of double tropopauses (DT) structures. The new method improves the definition of cold point tropopause, and detects one (or two) most significant local coldest point(s) by fitting the temperature profiles to the bi-Gaussian function, which is (are) defined as the tropopause height(s). The bi-Gaussian function exhibits remarkable potential for explicating the variation trend of temperature profiles. The recognition results of the bi-Gaussian method and lapse rate tropopause, as defined by World Meteorological Organization, are compared in detail for different cases. Results indicate that the bi-Gaussian method is able to more stably and obviously identify the spatial and temporal distribution characteristics of the thermal tropopauses, even in the presence of multiple temperature inversion layers at higher elevations. Five-year (from 2012 to 2016) historical radiosondes in China revealed that the occurrence frequency and thickness of DT, as well as the single tropopause height, and the first and second DT height displayed significant meridional monotonic variations. The occurrence frequency (thickness) of DT increased from 1.07 % (1.96 km) to 47.19 % (5.42 km) in the latitude range [16 ºN, 50 ºN]. The meridional gradients of tropopause height were relatively large in the latitude range of [30 ºN, 40 °N], essentially corresponding to the climatological location of the subtropical jet and Tibetan Plateau. DT structure occurs most frequently and has the largest meridional gradient in the mid-latitudes, formatted by a combination of poleward advection in the low-latitude upper troposphere and equatorward advection in the high-latitude lower stratosphere. In addition, although DT is thick in winter, the DT temperature difference is small, even the case of the first tropopause temperature is lower than the second tropopause temperature happens occasionally.

1 Introduction

As a pivotal transitional layer uniting the troposphere and stratosphere, there are complex multi-scale atmospheric physicochemical coupling processes in the tropopause layer, such as atmospheric radiation and dynamical processes (Fueglistaler et al., 2009; Gettelman et al., 2011). The tropopause is a transitional layer between the upper troposphere-lower stratosphere (UTLS), mainly manifesting in the transportation of atmospheric energy and masses to the stratosphere through this "gate" and further advection and diffusion (Yang and Lv, 2004; Fueglistaler et al., 2009; Holton et al., 1995). The long-time variations of the tropopause thermal and dynamic structures are regarded as crucial indicators of climate change (Santer et al., 2003b; Santer et al., 2003a; Sausen and Santer, 2003; Xian and Fu, 2017; Seidel et al., 2001; Shepherd, 2002; Seidel and Randel, 2006; Thompson et al., 2021; Meng et al., 2021). However, the comprehension of the fine tropopause structures is still limited (Bian et al., 2020), leading to varying degrees of biases in the tropopause inversion layer characteristics analysis (Randel et al., 2007b; Wang et al., 2013) and climate model simulations (Li et al., 2020; Sun et al., 2021; Tian et al., 2017; Xian and Fu, 2015; Maddox and Mullendore, 2018).

It is beneficial to understand the formation mechanisms of tropopause, formatted by the combination of tropospheric and stratospheric processes, and to further research stratosphere-troposphere exchange (STE) processes by defining the tropopause from various perspectives. Reviews of existing tropopause definitions and their performances were summarized by Maddox and Mullendore (2018), Tinney et al. (2022), and Boothe and Homeyer (2017). In early atmospheric models, the tropopause is characterized as a discontinuous interface featuring a sharp vertical gradient. Reed (1955) proposed the concept of dynamical tropopause and discovered the tropopause folding events. Later, the dynamic tropopause was defined based on the zero-order discontinuity of potential vorticity (Danielsen et al., 1987). Based on the vertical structure of atmospheric temperature and the characteristics of a sharp decrease in the temperature lapse rate, the World Meteorological Organization (WMO) defined the lapse rate tropopause (LRT) (WMO, 1957). From a chemical point of view, Bethan et al. (1996) analysed whether there was a saltus in the atmospheric tracer concentrations through the thermal and dynamic tropopause, and set a threshold of the vertical gradient of ozone mixing ratio to represent the ozone tropopause (Pan et al., 2004; Pan et al., 2014; Ma et al., 2022). Recently, a stability–based potential temperature gradient tropopause (PTGT) definition was developed to identify the greatest composition change within the tropopause transition layer (Tinney et al., 2022).

It is more reasonable to consider the tropical tropopause as a transition layer than a discontinuous interface (Highwood and Hoskins, 1998). Gettelman and Forster (2002b) comprehensively considered both radiation and convection, and separated cold point tropopause (CPT) and potential temperature lapse minimum rate (LRM) tropopause as the upper and lower boundaries of tropical tropopause layer, respectively. A primary characteristic of the tropopause is the drastic alteration of the atmospheric static stability when crossing this transitional layer. To estimate the thickness of tropopause layer, atmospheric static stability parameter buoyancy frequency N has been used, characterized by the vertical potential temperature gradient (Homeyer et al., 2010). Static stability undergoes a discrete jump from low value (unstable) in the troposphere to high value (stable) in the stratosphere (Birner, 2006; Gettelman and Wang, 2015; Bai et al., 2017).

The meridional distribution of the thermal tropopause height, ranging from tropical to subtropical latitudes, often exhibits a discontinuous variation, called "tropopause break" (Randel et al., 2007a; Rieckh et al., 2014; Schmidt et al., 2004; Palmen, 1948; Xian and Homeyer, 2019). Coincidentally, in the overlapping tropical and mid-high latitudes, adjacent to the subtropical jet (STJ), double tropopauses (DT) are frequently formed (Randel et al., 2007a; Xian and Homeyer, 2019; Schmidt et al., 2006). Fluctuations in atmospheric temperature resulting from different atmospheric circulation systems, such as the Asian summer monsoon and polar vortex, can cause abnormal changes of tropopause height and increase the possibility of DT formation (Randel et al., 2007a; Rieckh et al., 2014; Ravindrababu et al., 2020; Shangguan et al., 2019). Currently, some studies have focused on atmospheric stability and tracers STE processes associated with the DT events, revealing that DT can impact the maximum water vapor levels and stratospheric hydration in the lower stratosphere, as well as ultimately ozone concentration, transported by convective overshooting (Randel et al., 2007a; Pan et al., 2004; Gamelin et al., 2022; Homeyer et al., 2014b; Homeyer et al., 2014a). DT has an important influence on the vertical distribution, transport, and diffusion of atmospheric compositions, with active STE, and is a non-negligible key transition layer when considering any mid-latitude stratosphere-troposphere activities (Peevey et al., 2014; Parracho et al., 2014; Liu and Barnes, 2018).

In order to deeply understand the coupling processes and triggering mechanisms involved in the UTLS, the evolution of the fine tropopause structures must be comprehensively understood. However, the results of the existing tropopause identification methods are quite different in some cases, and the formation mechanism and evolution process of DT and tropopause inversion layer are still active areas of research. Therefore, it is imperative to find a reliable and highly universal method to identify the characteristic parameters of tropopause vertical structures (Bian et al., 2020; Tian et al., 2017).

The objective of this study is to introduce a new method to identify the multiple characteristic parameters of tropopause vertical structure. The temperature profiles obtained from radiosondes have been utilized to be fitted by a bi-Gaussian function, which can not only identify the tropopause height and tropopause temperature, but also express the information of DT structure, such as the thickness, as well as effectively assisting characteristic analysis on tropopause inversion layer. The key aspects of this work are outlined as follows: Sec. 2 presents an account of historical radiosondes used in the study, commonly utilized definitions of thermal tropopause in previous researches, as well as a thorough description of the new identification method based on the bi-Gaussian function in details. The feasibility analysis of the new method, and comparisons with the existing definitions are highlighted in Sec. 3. In Sec. 4, a comprehensive discussion of the spatiotemporal characteristics of the tropopause structures in China based on this new bi-Gaussian method is provided. The reasons for the formation of the DT structure in the mid-latitudes and its vertical structure characteristics are discussed in Sec. 5. Ultimately, conclusions are summarized in Sec. 6.

2 Data and methods

2.1 Radiosondes
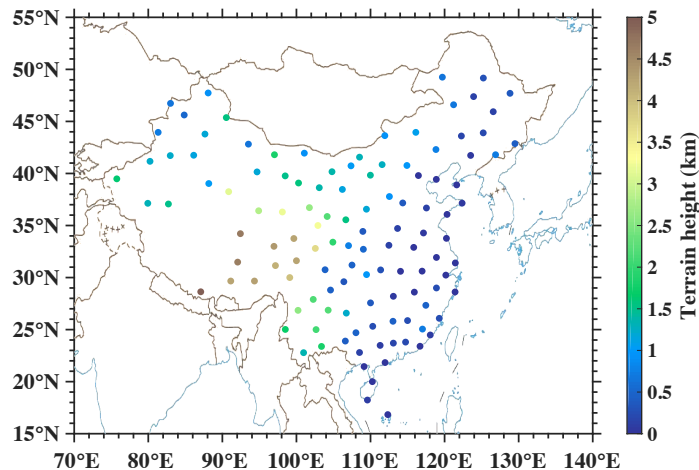
95

Figure 1: Spatial distribution of sounding sites (dots) and relevant terrain heights (color-coded). The map is provided by the official website of the Ministry of Natural Resources of the People's Republic of China, NO: GS (2016) 1667 (the same as below).

Despite there are numerous studies on the tropopause structures based on satellite data (Alexander et al., 2011; Liu et al., 2019; Rieckh et al., 2014), radiosonde observations of air temperature, the traditional and most widely used, are crucial and essential for studying the fine tropopause structures (Chen et al., 2006; Xian and Homeyer, 2019; Seidel et al., 2001). The historical radiosondes were obtained from 120 sounding sites (color-coded in Fig. 1) in China, covering tropical, subtropical, temperate and plateau climate zones, from 2012 to 2016, as described in detail in Guo et al. (2016). Once- or twice- daily radiosondes, launched at 08:00 and 20:00 (local time), throughout four seasons have a higher vertical resolution (about 5 to 8 m) than reanalyses, providing an excellent opportunity for a more precise identification of tropopause height, temperature, and DT structures. The basic information on the temperature profiles from radiosondes is listed in Table 1.

Table 1: Information for high-resolution temperature profiles from radiosonde measurements.

Launch time	08:00 and 20:00 (local time)
Sampling time	1 s
Vertical resolution	5 to 8 m
Measurement range	−90 to 50 °C
Temperature accuracy	≤0.2 °C (−70 to 50 °C)
	≤0.3 °C (−90 to 80 °C)

2.2 Reanalysis

The stratospheric polar vortex is a large-scale circulation system over the polar region in the Northern Hemisphere winter, which is related to tropospheric circulation anomalies and plays an important role in the stratosphere–troposphere coupling (Ren and Cai, 2007; Zhang et al., 2016; Liang et al., 2023). The polar vortex intensity is defined as (Kolstad et al., 2010),

$$-Z_P = -\sum (Z' \cos \varphi) / \sum \cos \varphi \tag{1}$$

$$Z' = Z - \bar{Z} \tag{2}$$

Where, Z and $\bar{Z}$ represent the 50 hPa geopotential height and its climatological mean, calculated during the period from January 1, 1961 to December 31, 2020, respectively. φ is the latitude, and the summation symbols denote the sums of all grid points north of 65 ºN. $-Z_P$ denotes the polar vortex strength index, which is opposite to the sign of the geopotential height anomaly in the polar region, as shown by the negative (positive) index corresponding to a weak (strong) polar vortex. The polar vortex is an interaction between the stratosphere and troposphere, which influences the wind, pressure, and temperature distributions in the Northern Hemisphere winter. This top-down circulation anomaly affects the winter climate anomaly in East Asia, and the weak polar vortex is more easily transmitted from the stratosphere down to the troposphere and have a significant effect on the tropospheric circulation, especially when the stratospheric outburst warming occurs in winter (Chen and Wei, 2009).

ERA5 daily reanalysis are used to analyze the potential influence of atmospheric circulation anomalies on the tropopause vertical structure (Hersbach et al., 2020), including geopotential height, potential vorticity (PV, units: PVU, 1PVU=10^{-6} m^2 K kg^{-1} s^{-1}), temperature, V-component of wind (V), vertical velocity (W), etc. The horizontal resolution of these parameters is 2.5º×2.5º, and there are 23 layers in vertical direction, including 850, 825, 800, 775, 750, 700, 650, 600, 550, 500, 450, 400, 350, 300, 250, 225, 200, 175, 150, 125, 100, 70, 50 hPa.

2.3 Previous thermal tropopause definitions

Five thermal tropopause definitions (CPT, LRT, LRM, PTGT, and curve fitting to N^2) are shown in Fig. 2, using the radiosondes at a tropical site (112.33 ºE, 16.83 ºN).
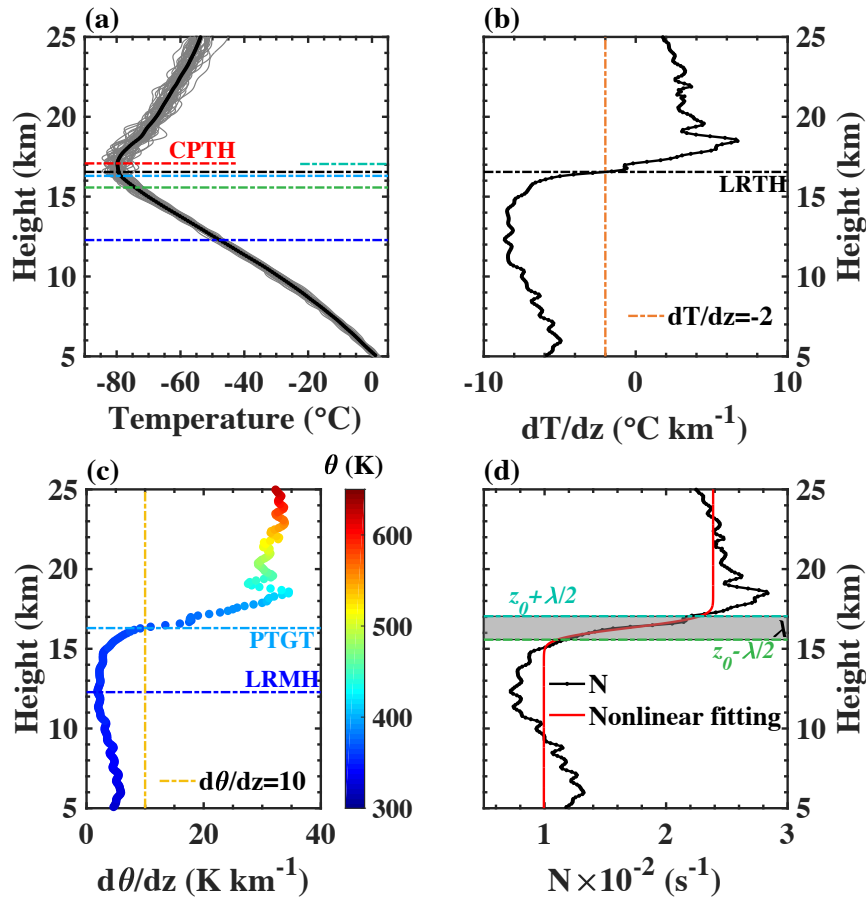
Figure 2: Five different thermal definitions were shown. A 15-point running mean was adopted for temperature and potential temperature profiles. (a) Comparisons of thermal tropopause heights detected from different definitions. The temperature profiles (grey lines) are sourced at a tropical site (112.33 ºE, 16.83 ºN) in July, 2014, and the black dotted line denotes the average temperature profile of 57 grey profiles. (b) temperature lapse rate profile and LRT, (c) potential temperature lapse rate profile, LRM, and PTGT, (d) curve fitting to N^2.

2.3.1 Cold point tropopause and potential temperature lapse rate minimum tropopause

The atmospheric stability within the tropical tropopause layer is affected by convection in the troposphere and radiation in the stratosphere (Gettelman and Forster, 2002b; Thuburn and Craig, 2002). CPT is the coldest point in the temperature profile and marks a sharp increase in stability, above which the potential temperature profile is close to radiative equilibrium (Gettelman and Forster, 2002a; Randel and Park, 2019; Pan et al., 2018; Pan et al., 2014). The CPT height (CPTH, in Fig. 2(a)) and LRM height (LRMH, in Fig. 2(c)) are also adopted to characterize the upper and lower boundaries of the tropical tropopause layer (Gettelman and Forster, 2002b; Alappattu and Kunhikrishnan, 2010; Seidel et al., 2001). CPTH almost coincides with the minimum saturated water vapor mixing ratio (Fueglistaler et al., 2009; Kley et al., 1979; Randel and Park, 2019), and stratospheric water vapor concentration is mainly determined by the tropopause temperature (Rosenlof and Reid, 2008;

Rosenlof, 2003; Xie et al., 2020). Furthermore, LRMH holds three physical meanings (Gettelman and Forster, 2002b; Ravindrababu et al., 2020):

1) The maximum height at which convection still affects temperature in the upper troposphere;

2) The height at which temperature begins to be influenced by stratospheric radiation;

3) It coincides with the height corresponding to the minimum ozone mixing ratio.

2.3.2 Lapse rate tropopause

The LRT defined by WMO is widely utilized (Liu et al., 2019; Randel et al., 2007a; Rieckh et al., 2014; Schmidt et al., 2006; Schmidt et al., 2004; Xian and Homeyer, 2019; Hoffmann and Spang, 2022; Feng et al., 2012). The LRT definition is as follows:

(i) The first tropopause is defined as the lowest level at which the lapse rate decreases to 2 °C/km or less, provided that the average lapse rate between this level and all higher levels within 2 km does not exceed 2 °C/km.

(ii) Above the first tropopause, if the average lapse rate between any level and all higher levels within 1 km exceeds 3 °C/km, then a second tropopause is defined using the same criterion as under (i). This tropopause may be either within or above the 1 km layer.

LRT is generally considered to be the most reliable definition because of the nearly universal applicability, as well as the ability to identify the approximate location of the sharpest gradient of stability and chemical compositions in the UTLS (Gettelman et al., 2011; Pan et al., 2018; Hoffmann and Spang, 2022). The WMO method described in the APPENDIX of Maddox and Mullendore (2018) was adopted to calculate the average lapse rate.

2.3.3 Curve fitting to Brunt-Vaisala frequency

The buoyancy frequency N^2 is an indicator of atmospheric static stability, which is characterized by vertical potential temperature lapse rate (Homeyer et al., 2010; Birner, 2006; Gettelman and Wang, 2015; Bai et al., 2017), as following:

$$N^2 = \frac{g}{\theta}\frac{\partial\theta}{\partial z}, \tag{3}$$

Where, g is the gravitational constant, θ is the potential temperature, and z is the altitude. A primary characteristic of tropopause layer is that the static stability changes drastically when crossing the tropopause layer. According to the discrete jump of N, N is fitted by nonlinear least square method (in Fig. 2(d)), proposed by Homeyer et al. (2010), to detect tropopause structures, as following,

$$N(z) = N_{\text{trop}} + \frac{N_{\text{strat}} - N_{\text{trop}}}{2}\left[1 + \text{erf}\left(\frac{2(z-z_0)}{\lambda}\right)\right], \tag{4}$$

Where, N_{trop} and N_{strat} are the asymptotic values of N in the troposphere and stratosphere respectively, z_0 is the mid-point of the tropopause height, λ is the thickness of the transition layer, and erf represents the error function. N_{trop}, N_{strat}, z_0 and λ can be obtained by nonlinear least squares fitting, with N_{trop}=0.0 s^{-1}, N_{strat}=25.0 s^{-1} and λ =1 km as the initial value of the

fitting, and z_0 calculated according to the definition of WMO. In order to reduce the fitting error, data with altitude lower than
175   5 km are discarded. Non-linear fitting of N can directly obtain the upper and lower boundaries of the tropopause layer (in Fig. 2(d)).

2.3.4 Potential temperature gradient tropopause

PTGT (in Fig. 2(c)), a modern stability-based tropopause definition was developed by Tinney et al. (2022) serves as an alternative to the LRT, provides additional insights for tracer–tracer stratosphere–troposphere exchange.
180

2.4 New bi-Gaussian method

It can be seen from Fig. 2 that the tropopause heights identified by the above five definitions are quite different in some cases (Wirth, 2000; Pan et al., 2018; Bian, 2009). Moreover, each definition is not universally employable, and most definitions hardly provide essential information about the transition layer structures.

185   CPT and LRT have good applicability in the tropics, mainly due to the simple terrain and minimal impact of weather systems intrusion. But, the limitations of these two definitions become apparent in the extratropics, as shown in Fig. 3(a). The blue cross-line represents the measured temperature profile, and red dot-line is temperature lapse rate. According to the WMO algorithm, points C and D represent the first and second LRTH (LRTH1 and LRTH2), respectively. Point B (CPTH) is quantitatively comparable with point D (LRTH2), however, CPT fails to identify point A, which corresponds to LRTH1 (point
190   C). Therefore, CPT is unable to characterize double tropopauses (DT) structure.
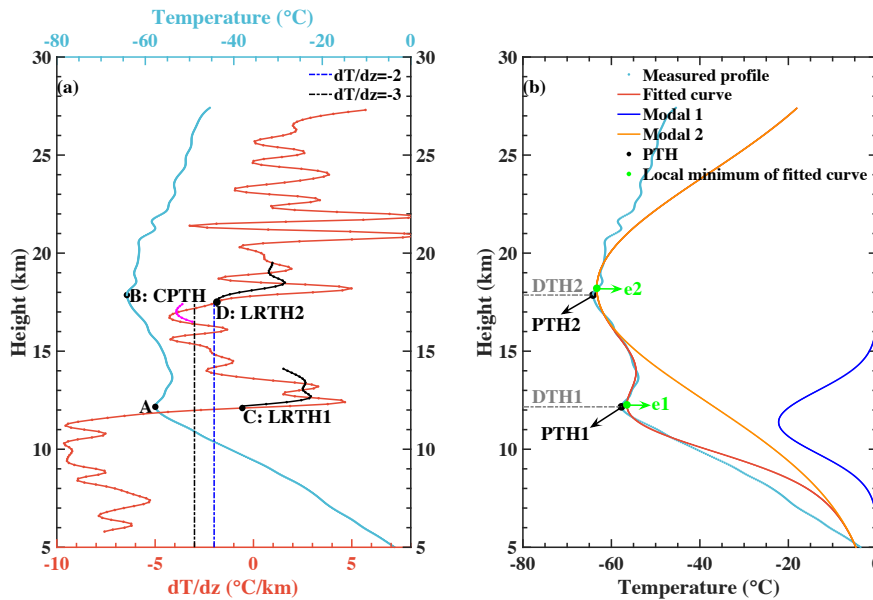
Figure 3: (a) Schematic diagram illustrating the limitation of the CPT. The temperature profile was sourced from a site (106.2 °E, 38.37 °N) at 12:20 location time 17 Jun 2014 (Local Time, the same below). Points C and D are defined by LRT. The black dotted line indicates "the average lapse rate between this level and all higher levels within 2 km", and the magenta dotted line indicates "the average lapse rate between any level and all higher levels within 1 km". (b) An example for bi-Gaussian function fitting to detect the tropopause heights. Above 15 km, Modal 1 equals zero, and Modal 2 perfectly coincides with the fitting curve.

Inspired by Fig. 3, both A and B represent local minimum points within a specific height range. Therefore, the local coldest point is used to replace the coldest temperature point in this study. The local coldest point is defined as follows: assuming that there exists a certain height h_0 (unit: km), where the temperature is the coldest in the interval $[h_0-1, h_0+1]$, we logically define h_0 as the possible tropopause height (PTH), hereinafter referred to as "target". The target-seeking range $[TH_{min}, TH_{max}]$ is confined to minimize the identification error, corresponding to the lower and upper limits of tropopause height, respectively, as following (Liu et al., 2021):

$$TH_{min} = 2.5 \times (3 + \cos(lat \times 2)) , \qquad (5)$$

$$TH_{max} = 2.5 \times (7 + \cos(lat \times 2)) , \qquad (6)$$

where, lat is the latitude of observation sites.

There are two reasons for constraining the search range.

1) to avoid unrealistically high or low tropopause heights and to increase computational speed (Reichler et al., 2003; Li et al., 2017).

2) What cannot be ignored is the presence of triple tropopauses, even if the occurrence frequency of triple tropopauses is very low. The third tropopause is mainly distributed at ~50 hPa (Anel et al., 2007; Xu et al., 2014). So, it is assumed that there are double tropopauses at most within the height interval $[TH_{min}, TH_{max}]$. An example can be referred to in Fig. S3 in the Supplement.
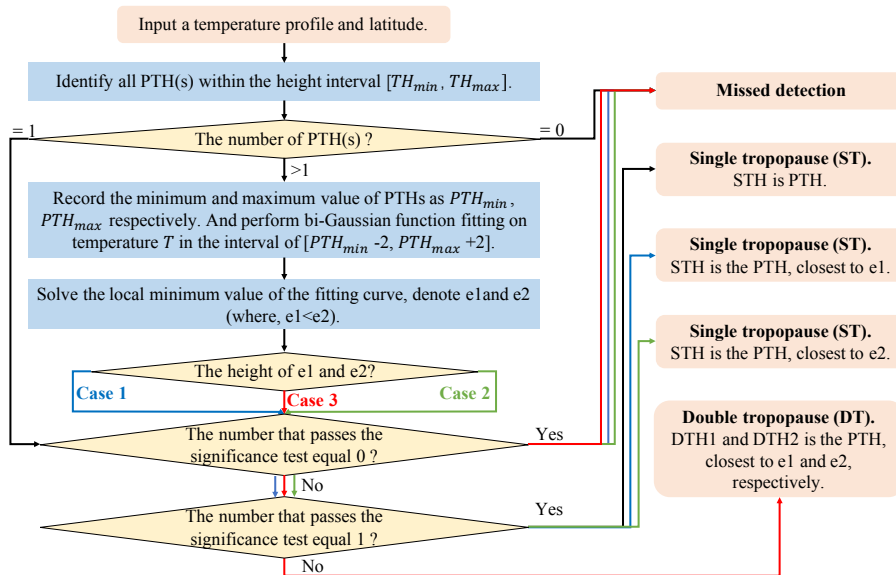
Figure 4: The flow chart for utilizing the bi-Gaussian function to fit temperature profiles for identifying the tropopause height and the DT structure. The judgment criteria of Case 1, Case 2 and Case 3 are listed in Table 2.

The detailed steps to identify the prominent target(s) are presented in Fig. 4, and the specific steps are delineated below.

1) **Target seeking**: Identify all PTH(s) within the height interval $[TH_{min}, TH_{max}]$. If the number of PTH(s) is equal to 1, proceed to step 4); otherwise, follow the subsequent steps.

2) **Curve fitting**: Record the minimum and maximum values of PTHs as PTH_{min} and PTH_{max}, respectively. Bi-Gaussian function fitting is performed on the temperature profiles in the height interval $[PTH_{min}-2,\ PTH_{max}+2]$. The function is expressed as Eq. (7), where $a1 * \exp\left(-\left(\frac{x-b1}{c1}\right)^2\right)$ and $a2 * \exp\left(-\left(\frac{x-b2}{c2}\right)^2\right)$ is called Modal 1 and Modal 2 of the bi-Gaussian function, respectively.

$$f(x) = a1 * \exp\left(-\left(\frac{x-b1}{c1}\right)^2\right) + a2 * \exp\left(-\left(\frac{x-b2}{c2}\right)^2\right), \tag{7}$$

3) **Conditional judgment**: Solve the local minimum points of the fitted curve, namely e_1 and e_2, and judge whether e_1 and e_2 are within the interval of $[PTH_{min}-2, PTH_{max}+2]$, respectively. If the result is true, it is considered a valid value; otherwise, it is an invalid value.

4) **Significance tests**: Ensure that the inversion layer strength, which is represented by the slope of linear fitting to the temperature profiles in the range of [valid PTH(s), valid PTH(s)+2], is not less than 0.5 °C/km (Randel et al., 2007b). Otherwise, it is invalid.

5) **Identification results**: Determine the PTH(s) closest to the final valid value(s), which is (are) the tropopause height(s) (In the following, the abbreviation STH specifically refers to the single tropopause (ST) height, and DTH1 and DTH2 refers to the first and second DT height, respectively).

Table 2: criteria in conditional judgments.

Conditional judgments	Criterion
Case 1	$(PTH_{min} -2 \leq e_1 \leq PTH_{max} + 2)$ is true & $(PTH_{min} -2 \leq e_2 \leq PTH_{max} + 2)$ is false
Case 2	$(PTH_{min}-2 \leq e_1 \leq PTH_{max} + 2)$ is false & $(PTH_{min}-2 \leq e_2 \leq PTH_{max} + 2)$ is true
Case 3	$(PTH_{min} -2 \leq e_1 \leq PTH_{max} + 2)$ is true & $(PTH_{min}-2 \leq e_2 \leq PTH_{max} + 2)$ is true

Fig. 3(b) shows an example of using the new method to identify tropopause heights, where h1 (PTH1) and h2 (PTH2) indicate the first DT height (DTH1) and the second DT height (DTH2), respectively. Table 3 summarizes the results and goodness of fit statistics from the bi-Gaussian function fitting to the temperature profile in Fig. 3(b).

The coefficient of determination R^2 is used to evaluate the performance of bi-Gaussian function,

$$R^2 = 1 - \frac{\text{SSE}}{\text{SST}}, \tag{8}$$

where, the sum of squares due to error $\text{SSE} = \sum_{i=1}^{n}(X_i - Y_i)^2$, and $\text{SST} = \sum_{i=1}^{n}(Y_i - \bar{Y})^2$, where X_i and Y_i is the fitting and measurement temperature profiles, respectively, and n is the number of samples.

Table 3: The results and goodness of fit statistics of bi-Gaussian function fitting to the temperature profile in Fig. 3(b).

	Fit parameters	Goodness of fit statistics	
$a1$	−8.451 (−9.349, −7.552)		
$b1$	9.158 (9.072, 9.244)	SSE	55.4310
$c1$	1.767 (1.609, 1.925)		
$a2$	−55.72 (−55.82, −55.61)		
$b2$	14.3 (14.07, 14.53)	R^2	0.9450
$c2$	17.72 (16.53, 18.91)		

3 Feasibility analysis of the bi-Gaussian method

78,758 temperature profiles in 2014 were employed to discuss the feasibility of the bi-Gaussian method, including the capacity of the bi-Gaussian function to effectively interpret the temperature profiles, and comparing with existing definitions.

245   ### 3.1 Explanation capability of bi-Gaussian function for UTLS temperature profiles
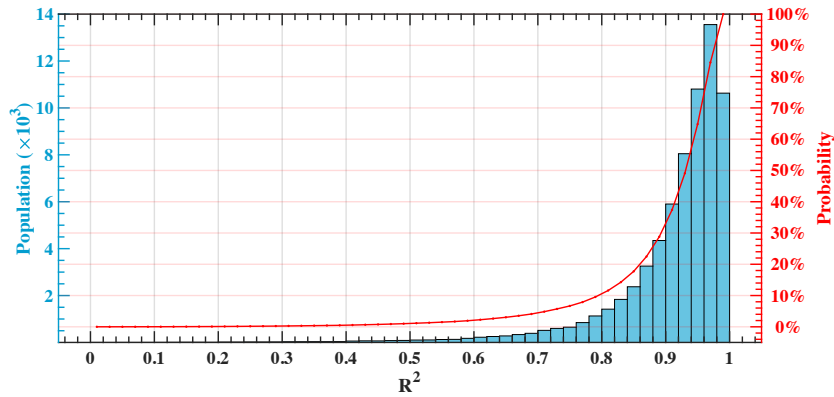
Figure 5: Goodness of fit statistics (the coefficient of determination R^2) for bi-Gaussian function fitting to temperature profiles and cumulative probability distribution.

Of the 78,758 temperature profiles, there are 68,896 profiles with no less than one PTH. Figure 5 shows the coefficient
250   of determination R^2, one of the fitting evaluation indexes, of the 68,896 temperature profiles fitted by bi-Gaussian function. Higher R^2 values indicate better goodness of the regression model. R^2 is greater than 0.8 in at least 90% temperature profiles, and the average R^2 of all profiles reaches 0.9. Consequently, the bi-Gaussian function exhibits remarkable potential for accurately explicating temperature profiles in the UTLS, ensuring that PTHs are successfully identified.

3.2 Comparisons of the identification results between the bi-Gaussian method and LRT

Table 4: Identification results of the bi-Gaussian and LRT. It is noticed that the search range is also limited to LRT. The percentages represent the proportion of temperature profiles in each case. "Missed detect" means that there is no value satisfying the definitions within the search range.

Identification results		Bi-Gaussian		
		Missed detect	ST	DT
LRT	Missed detect	85 (0.11 %)	174 (0.22 %)	67 (0.09 %)
	ST	758 (0.96 %)	54,935 (69.75 %)	**8,682 (11.02 %)**
	DT	257 (0.32 %)	**4,439 (5.64 %)**	9,362 (11.89 %)

The tropopause structures of 78,758 profiles, identified using two methods, are summarized in Table 4. Limiting the search range can lead to missed detection (Li et al., 2017), an example shown in Fig. S1 in the Supplement. However, if the search range is expanded, both methods can get effective identification results. A total number of 77,417 profiles have been successfully identified. In general, the DT detection rate of bi-Gaussian and LRT is 27.69 % and 16.89%, respectively.
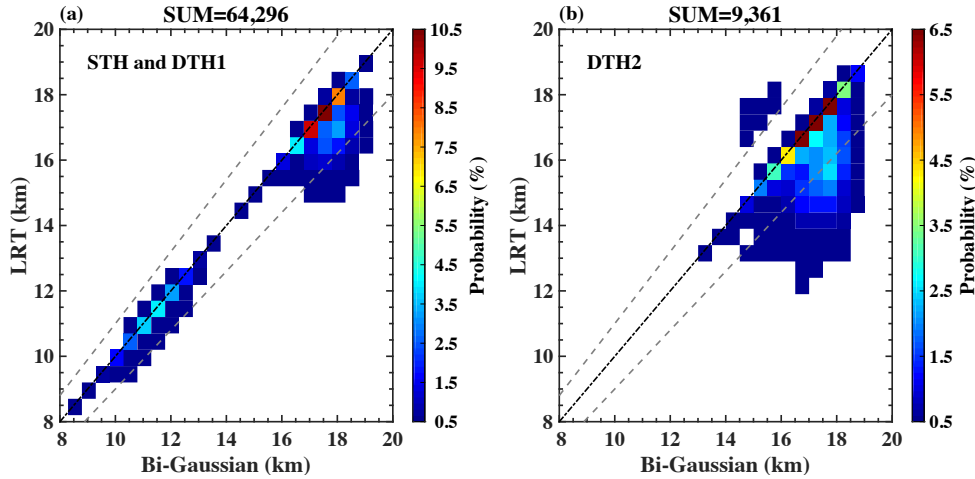
Figure 6: Comparison of identify results between the new bi-Gaussian method and LRT, the fill colormap represents the number of points, and the gray dotted lines indicate the 10 % error threshold; (a) STH and DTH1; (b) DTH2

Figure 6 shows the comparison of the identification results obtained through the new bi-Gaussian method and LRT. Both methods can identify 81.75 % cases with the same structural types. Specifically, the correlation coefficient (root mean square error) of the two methods for the STH and DTH1 is 0.93 (1.21 km) (in Fig. 6(a)), and at least 95 % of profiles' error between the two methods is no more than 10 %. There is a discontinuity at 14 km, which is called "tropopause break". Although the second DT height identified by the two methods are characterized by a more dispersed distribution (in Fig. 6(b)), 66.67 % of profiles have a percentage difference of no more than 10 % with the majority of the distribution are located on the line y=x, and the root mean square error is 1.7 km. Further, DTH2 identified by the bi-Gaussian are general higher than LRTH2 for 3,120 profiles.
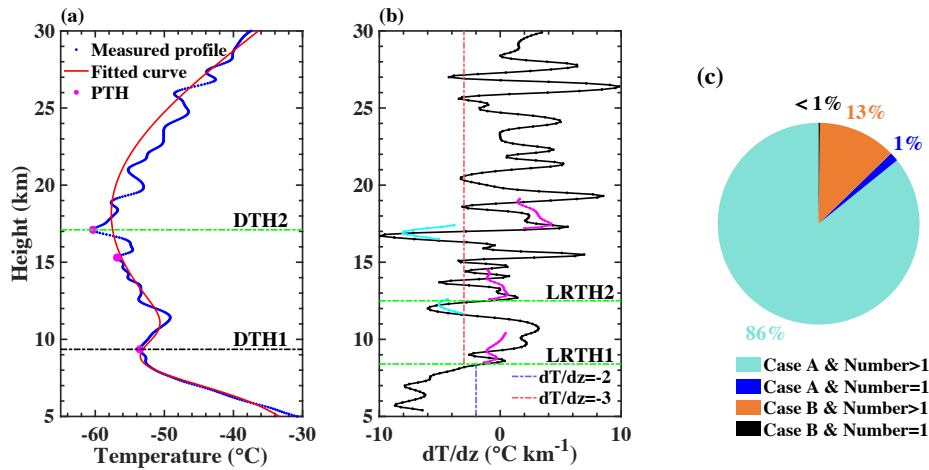
Figure 7: The characteristics of the 3,120 temperature profiles, which hold a difference of more than 10 % in the second DT height
275 **between the bi-Gaussian and LRT. (a) A typical profile to illustrate the possible reasons for the difference. The temperature profile**
was sourced from the site (121.22 °E, 46.6 °N) at 07:20 local time 13 Nov 2014; (b) temperature lapse rate profile and LRTH, The
magenta dotted line indicates "the average lapse rate between this level and all higher levels within 2 km", and the cyan
dotted line indicates "the average lapse rate between any level and all higher levels within 1 km"; (c) According to the
number of inversion layer(s) above the first tropopause and whether there is a higher and colder PTH, the 3,120 profiles are classified
280 **into four distinct clusters. These clusters are deliberated for the purpose of gathering characteristic statistical information. (Case A**
indicates the presence of a higher and colder PTH, and Case B is the converse of Case A).

Figure 7 shows the characteristic statistical analysis of the 3,120 temperature profiles with significantly different second

DT height (a percentage difference of more than 10 %) between the bi-Gaussian and LRT. A typical temperature profile (in

Fig. 7(a)) is exampled to illustrate the possible reasons for the difference in the second DT height between the two methods.

285 This typical profile displays two obvious characteristics. Firstly, two inversion layers are formed above the first tropopause,

meaning that there may be no less than one point that fit the criteria of the second tropopause height as defined by LRT.

Consequently, LRTH2 may be ambiguous due to the existence of multiple inversion layers (Hoerling et al., 1991). Secondly,

it is evident that at least one colder PTH above the first tropopause, frequently accompanied by a more significant temperature

inversion layer. Notably, the temperature of two PTHs (cyan dots) are lower than the first tropopause temperature. For the

290 3,120 profiles, more than 99 % profiles possess at least one of the features (in Fig. 7 (c)), and even 86 % possess both features

simultaneously. Among them, about 99 % profiles exhibit multiple inversion layers above the first tropopause.
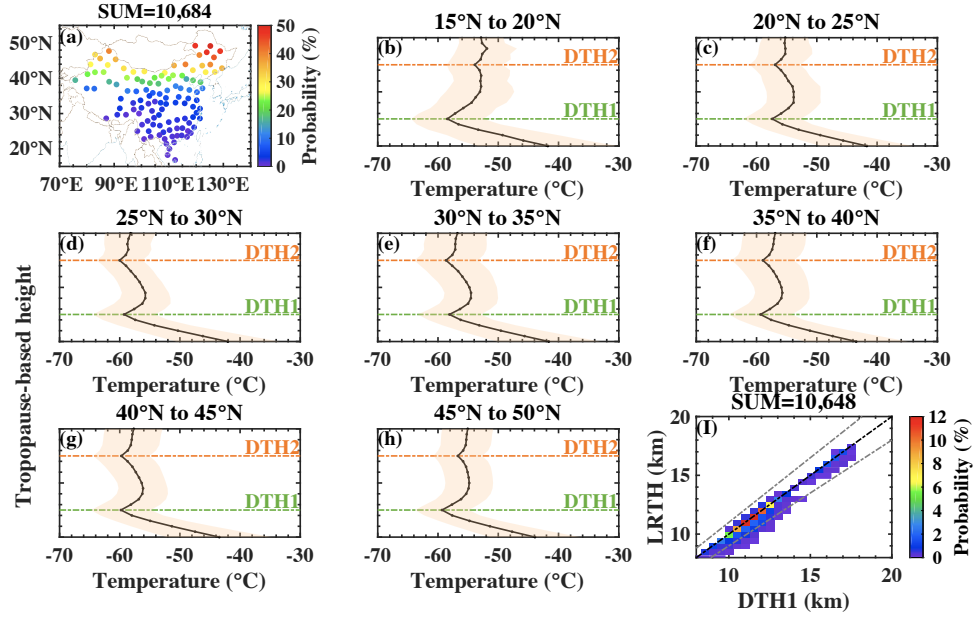
Figure 8: The cases that were identified as DT by the bi-Gaussian method but only ST by LRT. (a) ratio (contradictory results/ all observation of this site) distribution for the 8,682 temperature profiles. (b) − (h) annual average temperature profiles in 5° latitude bands. A tropopause-based height is adopted by using (DTH1+ DTH2)/2 as a reference level. (I) the comparison of DTH1 by bi-Gaussian and LRTH for the 8,682 profiles.

There are 14,377 temperature profiles with contradictory results from the LRT and bi-Gaussian method, of which the largest proportion (8,682 profiles) is identified as DT by bi-Gaussian method, but only ST by LRT. Fig. 8 shows the sites distribution of the 8,682 temperature profiles (bolded in Table 4) and the annual average temperature profiles with normalized height in each latitude zone. Using (DTH1+ DTH2)/2 as a reference level, the tropopause-based annual average temperature profiles of each latitude zone (in the interval of 5°) are calculated, as shown in Fig. 8(b) − (h). It can be clearly noticed that there is an inversion layer at both DTH1 and DTH2, and the strength of the inversion layer at DTH2 is significantly weaker than that at DTH1, and the bimodality is more pronounced at middle and high latitudes. LRT often fails to capture the weak stability transition (Tinney et al., 2022). The temperature lapse rate between DTH1 and DTH2 is mainly distributed in [–1.26 °C/km, –2.54 °C/km], not satisfying 'the average lapse rate between any level and all higher levels within 1 km exceeds 3 °C/km'. Therefore, the LRT definition of the second tropopause is not satisfied and defines these cases as ST. As can be seen from Fig.2 (I), LRTH is significantly consistent with DTH1, indicating that LRT could accurately identify the first tropopause, although fail to identify the second tropopause. Admittedly, the threshold of 0.5 °C/km in the significance tests might account for this contradictory. Below, we describe the reasons for choosing 0.5 °C/km as the threshold.
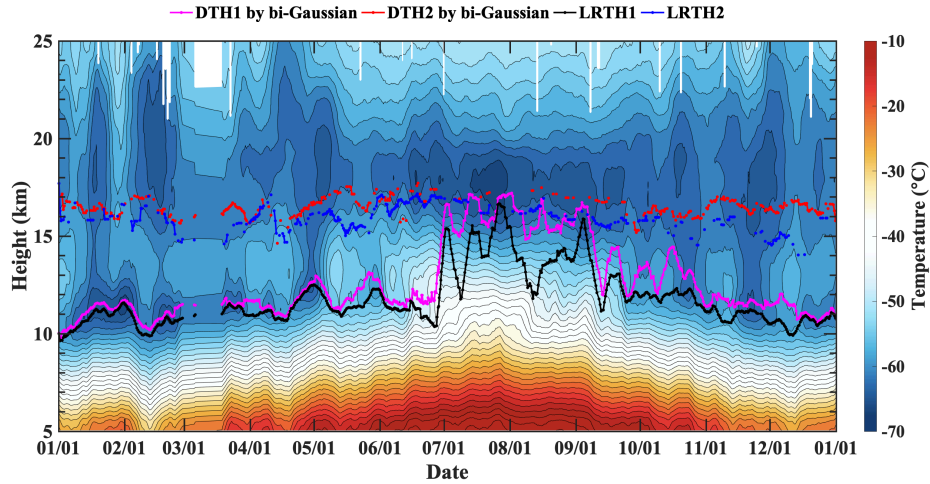
Figure 9: Temperature profiles from radiosondes in 2014 at Kuqa site (119.7 ºE, 49.25 ºN).

The evolution of the temperature field at the Kuqa site (119.7 ºE, 49.25 ºN) in 2014 is shown in Fig.9. There are obviously two local temperature minimum layers from January to May along the vertical direction, and the DT structure occurs frequently. With the increase of the surface temperature, the lower local temperature minimum layer was elevated from June to September, prevailing ST structure. After October, it re-evolved into two local temperature minima layers, prompting the formation of DT structures. The DT structures identified by Bi-Gaussian are mainly concentrated in winter and spring, while LRT identified a large proportion of DT structures from May to September. Therefore, the identification results of bi-Gaussian are more reasonable and more consistent with the evolution process of atmospheric thermal stratifications. In addition, the upper local temperature minima in November and December are too weak to be detected by LRT.

Bi-Gaussian function has a good ability to express the temperature profiles in the UTLS, and is able to more stably and obviously identify the spatial and temporal distribution characteristics of the thermal tropopauses. If a higher threshold is set, some DT structures are difficult to identify, as well as the LRT. As shown in the Fig.9, the threshold of 0.5 ºC/km ensures that bi-Gaussian has a good ability to identify the weak inversion layers. Fig.9 also reflects the differences in the recognition results of the two methods (as listed in Table 4). The LRT identified more DT structures in summer than bi-Gaussian, while the opposite was true in winter.

Similarly, there are 4,439 temperature profiles (bolded in Table 4, not shown) being identified as DT and ST by the LRT and new method, respectively. However, there is a single PTH in the bi-Gaussian function fitting curve within the range of $[TH_{min}, TH_{max}]$, expressing a more significant inversion layer. An example can be referred in Fig. S4.

3.3 Improvement of bi-Gaussian over CPT
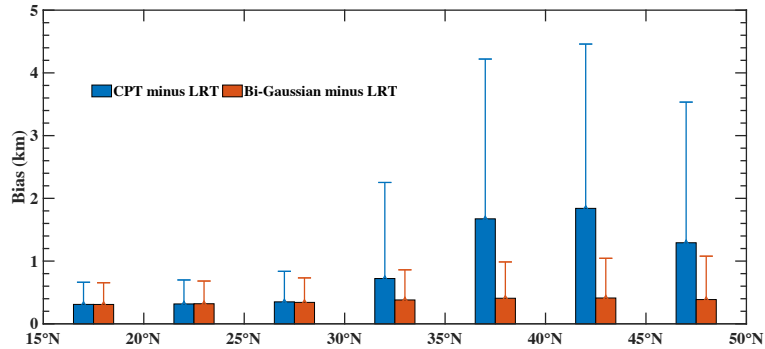
330

Figure 10: The biases of bi-Gaussian and CPT against LRT in different latitudes.

The CPTH and LRTH are inconsistent, with a positive bias of about [300 m, 2000 m] (Pan et al., 2018; Xia et al., 2021; Schmidt et al., 2004). On the one hand, the difference is caused by the inherent properties of the two definitions (see the Fig. S5), because CPTH is the transition point at which temperature lapse rate changes from negative to positive, which is common

335 in the tropics. On the other hand, CPT defines the higher and colder inversion layer (if exist) as the tropopause, so that the two methods can't identify the same temperature inversion layer (see Fig. 3(a)). This situation mostly occurs in the middle and high latitudes, which may be one of the reasons for the large bias between CPT and LRT in the middle and high latitudes.

CPT definition has better applicability in the tropics because of the simpler vertical thermal sturcture in the tropics, with fewer inversions. CPT can only return one identification result for both single and multiple structures, which is exactly why

340 CPT cannot identify multiple structures. Therefore, we define the local coldest point(s) instead of CPT in the new bi-Gaussian method as the possible tropopause height(s), and only the local coldest point(s) that have passed the significance test are considered to be the tropopause heights.

Compared with CPT, bi-Gaussian improves accuracy. Specifically, bi-Gaussian can not only identify the DT structures, but also identify the same temperature inversion layers as LRT. The identification results of bi-Gaussian have less bias against LRT, as shown in Fig.10. The bias between CPT and LRT is distributed at [0.31 km, 1.84 km], while the bias between bi-

345 Gaussian and LRT is stably at 0.37 km, even at mid-latitudes.

4 Spatiotemporal characteristics of tropopause structures in China

4.1 Double tropopauses structures: occurrence frequency and thickness
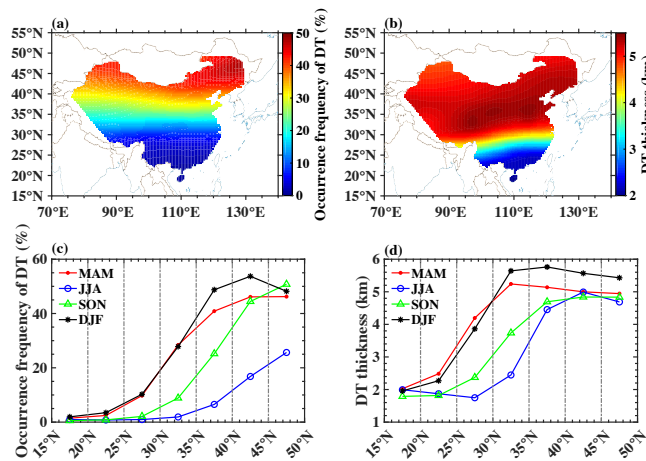
Figure 11: The meridional distribution of the annual (a, b), seasonal (c, d) mean occurrence frequency (a, c), and thickness (b, d) of DT in China during 2012−2016. Zonal means were determined for 5° latitude bins, and the same below.

In general, the occurrence frequency in Fig. 11(a) (thickness in Fig. 11(b)) of DT reaches its maximum in the Northern China and gradually decreases towards the tropics, showing typical meridional distribution characteristics (Schmidt et al., 2006; Seidel and Randel, 2006; Johnston and Xie, 2020). The maximum of annual mean occurrence frequency (thickness) is about 47.19 % (5.42 km), and the minimum is about 1.07 % (1.96 km) in the latitude range of [16 °N, 50 °N]. Additionally, the annual mean occurrence frequency in the latitude range of [30 °N, 45 °N] is about 28.93 %, which is roughly 7.51 times the occurrence frequency (3.85 %) in the latitude range of [20 °N, 30 °N]. The phenomenon that DT occurs frequently in mid-latitudes has also been recorded in previous studies and explained as the influence of the subtropical jet (STJ) system, whose mean climatological distribution position is about [30°, 45°] (Schmidt et al., 2006; Seidel and Randel, 2006).

Fig. 11(c) shows the zonal mean occurrence frequency of DT, determined for 5° latitude bins, in spring (March-April-May, MAM), summer (June-July-August, JJA), autumn (September-October-November, SON) and winter (December-January-February, DJF). Taking 30 °N as the dividing line, the DT occurrence frequency increases sharply from low to middle latitudes, particularly in winter and spring. DT occurrence frequency is not only low (<10 %) but also no significant seasonal variations in low latitudes. However, it shows obvious seasonal differences in middle latitudes, reaching the largest (~27.82 %−53.71 %) and the smallest (~1.89 %−25.65 %) in winter and summer, respectively. The mean climatological location of STJ gradually moves southward from [40 °N, 45 °N] in summer to [30 °N, 35 °N] in winter (Holton, 2004), and concurrently becomes stronger. In consequence, a large meridional gradient of DT occurrence frequency usually occurs in the climatological location of STJ and its adjacent latitude zone (±5°). DT occurrence frequency in the latitude range of [45 °N, 50 °N] does not maintain an increasing trend in winter, showing a downward trend, which is consistent with the result in (Randel et al., 2007a; Schmidt et al., 2006). However, such downward trends are not observed during other seasons.

In Fig. 11(b) and Fig. 11(d), the annual and seasonal mean DT thickness are consistent with previous study (Schmidt et al., 2006), maximizing in the latitude region of [30 °N, 50 °N]. The atmospheric temperature in UTLS over the northern China, especially in the mid-high latitudes, is primarily affected by cold air intrusion caused by weather systems, such as the Siberian High, the polar vortex, and the Asian winter monsoon (He and Wang, 2016; Woo et al., 2015; Shangguan et al., 2019).

375 Strengthened north winds are conducive to the advection and subsidence of cold air into East Asia, resulting in the hot and cold currents converge in the upper troposphere, which is beneficial to form significant temperature inversion layers.

4.2 Tropopause heights
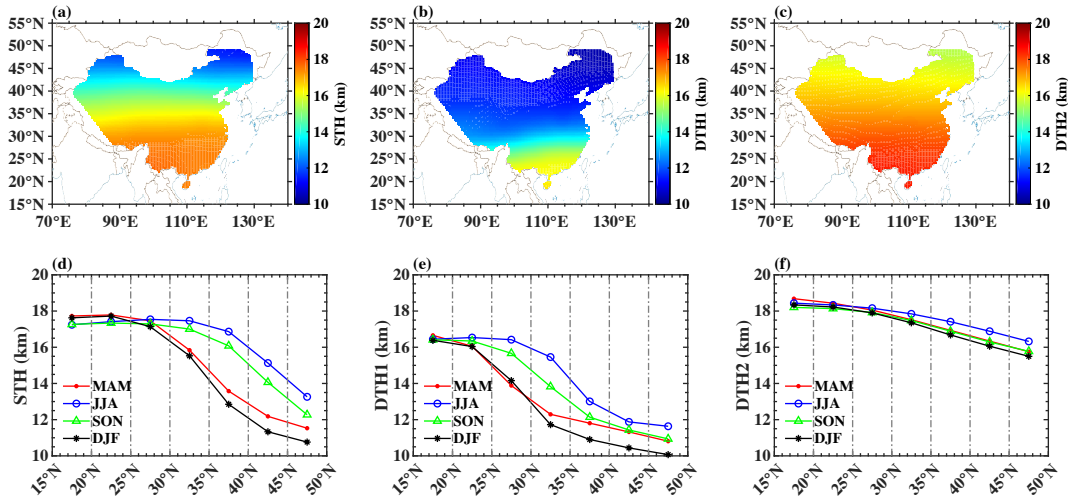
Figure 12: The meridional distribution of the annual and seasonal mean tropopause height in China during 2012−2016. The first
380 **row corresponds to the annual mean STH (a), DTH1 (b), and DTH2 (c). The second row represents the seasonal STH (d), DTH1 (e), and DTH2 (f) in spring, summer, autumn, and winter, respectively.**

As shown in Fig. 12, STH, DTH1 and DTH2 also manifest a significant meridional structure, which is similar to LRTH (Schmidt et al., 2004) and CPTH (Tang et al., 2017). STH (DTH1, DTH2) gradually decreased from 17.74 km (16.55 km, 18.50 km) to 11.43 km (10.43 km, 15.51 km) in the latitude range of [16 °N, 50 °N], with DTH2 appearing to display a weaker
385 meridional variation. The meridional distribution of tropopause height from tropical to subtropical regions is discontinuous, is known as the "tropopause break", corresponding to the zone with high DT occurrence frequency (Randel et al., 2007a; Rieckh et al., 2014; Schmidt et al., 2004; Feng et al., 2012; Xian and Homeyer, 2019; Pan et al., 2004).

The meridional gradients of STH, DTH1 and DTH2 in the latitude range of [30 °N, 40 °N] are significantly larger (in Fig. 12(d)−(f)), which basically corresponds to the climatological location of STJ and Tibetan Plateau. The tropopause structures
390 in the mid-latitudes are asymmetrical in both hemispheres (Xu et al., 2014), with a greater complexity in the Northern hemisphere (Xia et al., 2021; Han et al., 2011). In the Northern hemisphere, the meridional gradient of the first tropopause height is steeper (slower) in summer (winter) (Randel et al., 2007a), and DT occurs more frequently (Johnston and Xie, 2020;

Schmidt et al., 2006; Zeng et al., 2017) than that in the Southern hemisphere. Tibetan Plateau, a source of gravity waves (Hoffmann et al., 2013; Khan et al., 2016), may be one of the contributors to the asymmetry between the northern and southern hemispheres. During winter, the subtropical westerly jet is located on the southern margin of the Tibetan Plateau (Chen et al., 2006). and atmospheric fluctuations triggered by topography, jet-stream or convection (De La Torre et al., 2004), manifesting as strong variations in static stability (Koch et al., 2005), increase the probability of forming an inversion layer at a lower height. In summer, a strong Asian summer monsoon anticyclone is prevailing under the thermal difference between sea and land (Xu et al., 2019; Park et al., 2009; Bian et al., 2020; Liu et al., 2017; Wu et al., 2016; Ma et al., 2023), which can destabilize atmospheric temperature stratification in UTLS by inspiring deep convection and monsoon circulations (Randel and Park, 2006). However, the contribution of the unique thermal and dynamic effects of the Tibetan Plateau in different seasons to the tropopause structures in local and surrounding regions need further study.

5 Discussion on the formation mechanism of double tropopause in mid-latitude region in winter

Potential vorticity (PV) is commonly used to define a dynamic tropopause definition, and a 2 PVU is often chosen to represent the tropopause in synoptic-scale studies (Gettelman et al., 2011; Kunz et al., 2011). PV considers both the atmospheric static stability and the three-dimensional horizontal motion, ensuring the continuity of the dynamical tropopause distribution over large temporal and spatial scales. Therefore, PV is a well–characterized tracer in the study of stratosphere–troposphere interactions (Kunz et al., 2011).

The conceptual model of tropical STE summarized by Holton et al. (1995) is now widely recognized. However, the extratropical mid-latitudes, with the sharp meridional gradients in the tropopause construes, have a complex atmospheric dynamic processes (Butchart, 2022), like the stratospheric polar vortex. Therefore, the stratosphere-troposphere coupling process and its conceptual model still need to be further studied (Huang et al., 2018). Previous studies (Kolstad et al., 2010; Tomassini et al., 2012) have identified an association between temperature anomalies in the Northern Hemisphere and the strength of stratospheric polar westerlies (Christiansen, 2001; Zhuo et al., 2022). Taking winter season as an example, we will discuss the analysis of potential causes contributing to frequent DT structures in the mid-latitudes.
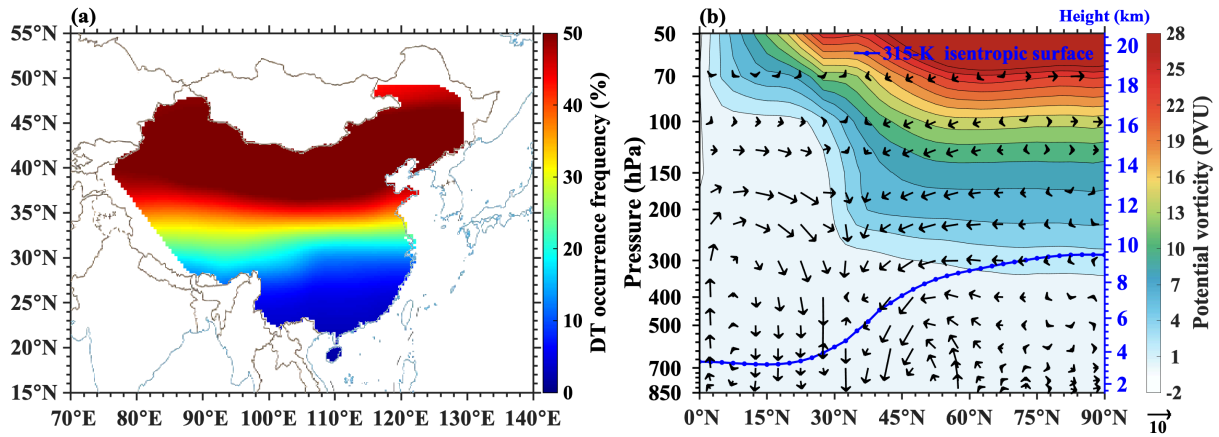
Figure 13: (a) Characteristics of the spatial distribution of DT occurrence frequency in China during the winter (DJF) from 2012 to 2016 based on radiosondes and the new Bi-Gaussian method; (b) Latitude–height cross section of PV (shading) and wind field (vectors, vertical velocity is scaled by –500) along the 75 °E–130 °E, and the blue dot line indicates the locations of the 315 K isentropic surface at different latitudes.

During the winter (DJF) from 2012 to 2016, the average DT occurrence frequency in the latitude range of [30 ºN, 50 ºN] (as shown in Fig. 13(a)) was about 45.2 %, decreasing sequentially from north to south. The maximum is concentrated in the latitudinal band of [40 ºN, 46 ºN], and decreases sharply in the latitudinal band of [30 ºN, 35 ºN], and the DT occurrence frequency in tropics is basically less than 10 %. As can be clearly seen from Fig. 13(b), significant poleward (equatorward) meridional advection exists south (north) of the mid-latitudes in upper troposphere (lower stratosphere) at low latitudes (high latitudes). The high PV (>4.5 PVU) and high static stability of the air masses creates equatorial advection on the isentropic surfaces (such as the 315 K isentropic surface, blue dot line in Fig. 13(b)) and invades over the mid-latitudes, called the "polar waveguide" (Zhang et al., 2022; Zhang et al., 2023). Upper tropospheric low PV (<2 PVU) and low static stability air mass carried by the polar advection, advecting to the middle latitudes above, called "low latitude waveguide". The north and south waveguides are advected at 100hPa and 300hPa layer respectively, causing PV anomalies that PV contour bows up and bows down at the high altitude of 30 ºN. As a result, the mid-latitudes act as a transition zone between warm and cold air masses, exhibiting discontinuities in temperature gradients. In addition, the 315 K isentropic surface has the largest downward tilt rate from 60 ºN to 30 ºN, corresponding to the region with the highest and the largest meridional gradient of the DT occurrence frequency, which indicates that the advection motions are closely related to the formation of DT structure.
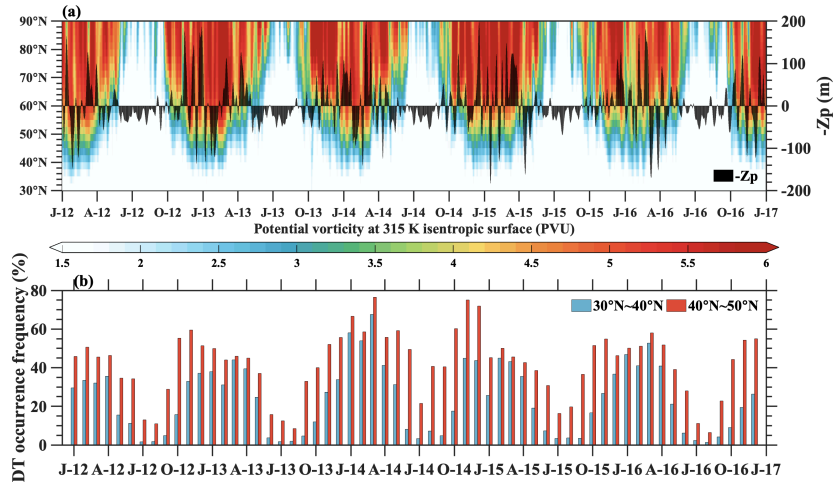
Figure 14: (a) Latitude–time cross section of the monthly mean potential vorticity at 315 K isentropic surface (shading) and daily $-Z_P$ (black bar; units: m) averaged along 75 °E–130 °E from January 2012 to December 2016; (b) the monthly mean DT occurrence frequency at the range of [30 °N, 40 °N] and [40 °N, 50 °N] based on radiosondes (along 75 °E–130 °E) from January 2012 to December 2016.

Fig. 14(a) shows the latitude–time cross section of the monthly mean PV at 315 K isentropic surface and daily polar vortex intensity $-Z_P$ from January 2012 to December 2016. Both the peaks and valleys of $-Z_P$ occur in winter, indicating the frequent and alternating occurrence of strong and weak polar vorticity. The tropopause height in the polar and high-latitudes is lower than that in the mid- and low-latitudes, so the height of the lower stratosphere (with a high PV) in the polar regions and high latitudes corresponds to the upper troposphere (with a low PV) in the mid-latitudes. Aforementioned trend, Fig. 14(a) vividly illustrates the southward movement (northward contraction, i.e., northward movement of tropical air masses) of polar (tropical) air masses in winter (summer). In winter, extremely cold air with high PV (>4.5 PVU) driven by polar vortex activities, invades southward along the sloping 315 K isentropic surface (Zhang et al., 2022; Zhang et al., 2023), even the 2 PVU contour line even crosses the 40 ºN. There was no similar pattern in summer.

The latitudinal band of [30 °N, 50 °N] is the tropopause break area, as well as the intersection area of polar and tropical air masses, which may be one of the reasons for the frequent DT structures in the mid-latitudes. In winter, the DT occurrence frequency in the [30 °N, 50 °N] latitudinal band reached 45.2 %, with the DT occurrence frequency in the [40 °N, 50 °N] latitudinal band being 51.55 %, which was higher than that in the [30 °N, 40 °N] latitudinal band (39.5 %). The higher DT occurrence frequency in the [40 °N, 50 °N] reinforces the impact of stratospheric polar vortex intrusion at high latitudes.

In the Northern Hemisphere, the stratospheric processes in the mid- and high-latitude during winter mostly are characterized by downward propagation to the lower troposphere (Christiansen, 2001), in which upper-level PV anomalies can vertically influence lower-level regions by regulating meridional circulations (Black, 2002). PV anomalies in the upper troposphere favor the southward movement of the accumulated cold Siberian air into the mid-latitudes, and then downward

transport, disrupting the vertical structure of atmospheric temperature and causing the discontinuities of temperature gradient. How does the above atmospheric circulation anomalies affect the characteristic parameters of DT vertical structures?
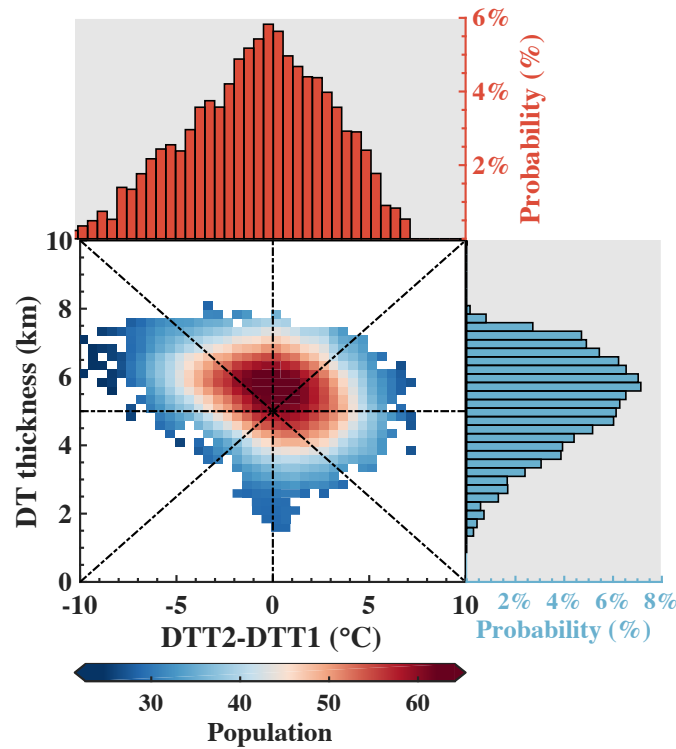
460

Figure 15: Frequency distribution between the DT temperature difference ΔT (= DTT2–DTT1, DTT1 and DTT2 denotes the first tropopause temperature and the second tropopause temperature, respectively) and the corresponding DT thickness for the [30 °N, 50 °N] latitude band (heatmap in the center). The upper and right histograms show the probability distribution of the ΔT, and DT thickness, respectively.

465 **Table 5: Statistics of tropopause heights and temperatures in the latitudinal band of [30 °N, 50 °N] during the winter from 2012 to 2016.**

	Tropopause height (km)			Tropopause temperature (°C)		
	STH	DTH1	DTH2	STT	DTT1	DTT2
Average	12.65	10.81	16.42	−62.38	−59.80	−62.13
Median	11.92	10.78	16.40	−62.04	−59.80	−61.36

Fig. 15 and Table 5 illustrate the statistical characteristics of the tropopause vertical structures (tropopause height, tropopause temperature and DT thickness) in the latitudinal band of [30 °N, 50 °N] during the winters from 2012 to 2016. ΔT (= DTT2–DTT1) and DT thickness are concentrated at [–3 °C, 3 °C] and [4 km, 7 km], and the mean values are −1.64 °C and

470 5.45 km, respectively. This means that even if there is a difference of 5.45 km between DTH2 and DTH1, DTT1 is lower than

DTT2 for 56.13 % profiles. The stratospheric high PV at high latitudes induces the stratospheric advection invasion of cold air from Siberia into the upper mid-latitude troposphere (Tomassini et al., 2012),especially when the inverted omega-shaped circulation pattern is formed, cold spells are very prone to break out (Zhang et al., 2022; Zhang et al., 2023). The convergence of warm and cold air not only forms a prominent thermal inversion layer at the first tropopause, but also drastically reduces the local minimum temperature, and even a few cases occur with DTT1<–65 °C (ΔT< –8 °C).

Why is DTH2 elevated and is DTT2 slightly larger than STT? The poleward warm advection in the upper troposphere at low–latitudes heats the upper atmospheric temperature in the mid-latitudes, increasing buoyancy and making an upward motion, which elevates DTH2 and increases DTT2. Anticyclonic vorticity is generated above the heat source, which is realized as negative PV anomaly. Combined with the positive PV anomaly, due to the advection invasion of equatorward high PV, this may increase the static instability within the deep tropopause layer, and intensifies atmospheric mixing and STE processes (Liu and Barnes, 2018).

6 Conclusions

This study presents a reliable and highly universal method for identifying tropopause structures, based on the concept of the local coldest point. Temperature profiles are fitted with the bi-Gaussian function to find the most significant one (two) local coldest point(s), which is (are) regarded as tropopause height(s). The bi-Gaussian function achieves a good explanatory potential for UTLS temperature profiles, ensuring that bi-Gaussian can reliably and stably capture the evolution of the tropopause, even for the weak inversion layers. This will benefit future STE studies and serves as an alternative to the previous thermal definitions. In addiation, the statistical analysis of the tracer-relationship based bi-Gaussian are being analyzed in the future research work to get further understanding, especially for the DT structures.

Five-year (from 2012 to 2016) historical radiosondes in China showed that tropopause structures (occurrence frequency and thickness of DT, STH, DTH1, and DTH2) displayed significant monotonous meridional distribution characteristics. In the latitude range of [15 ºN, 50 ºN], STH (DTH1, DTH2) gradually decreases from 17.74 km (16.55 km, 18.50 km) to 11.43 km (10.43 km, 15.51 km), and DT occurrence frequency (thickness) increased from 1.07 % (1.96 km) to 47.19 % (5.42 km), with a steep variation in middle latitudes. Subtropical regions [15 ºN, 25 ºN] exhibit ST-dominated conditions throughout the year, while mid-high latitudes [15 ºN, 35 ºN] experience high frequency of DT occurrence, particularly in winter where the occurrence frequency exceeds 50 %. This may be related to STJ activities and the intrusion of cold air from the north, caused by weather systems in winter. Notably, the climatic location of STJ and its adjacent latitude zone (±5º) exhibits a sharp increase in occurrence frequency. Furthermore, the DT thickness in the mid-high latitudes during winter is not less than 5 km. Moreover, tropopause structures over the Tibetan Plateau differ from those in the same latitudinal zone, likely due to unique atmospheric circulation structures such as the Asian summer monsoon anticyclone, planetary wave breaking and uploading, orographic gravity waves, and atmospheric temperature disturbances in the UTLS. However, the underlying mechanisms require further investigation.

Finally, the conceptual model of DT formation in the mid–latitudes during the winter is summarized. The deep DT structure is formed by the combined action of significant poleward and equatorward meridional advection. Meridional advection, driven by the polar vortex, of high–PV cold air from the polar regions and high latitudes into the mid–latitudes forms DT1 while cooling DTT1. On the other hand, the poleward advection of low-latitude waveguide in the low–latitudes upper troposphere elevates the DTH2 while warming DTT2.

Data availability. The radiosonde data used in this study are available upon the reasonable request from the corresponding author (luotao@aiofm.ac.cn).

Author contributions. KZ and TL jointly developed the concept of this study, and wrote the manuscript. XL prepared the radiosonde data. NW, YH, and YW conducted the data analysis, and contributed to the interpretation of the results. SC gave the financial support. All authors have read and agreed to the published version of the manuscript.

Competing interests. The authors declare that they have no conflict of interest.

Acknowledgements. This research has been supported by the Project funded by China Postdoctoral Science Foundation (Certificate Number: 2023M733537), the Foundation of Advanced Laser Technology Laboratory of Anhui Province (Grants no. AHL2022QN02, AHL2021QN01), the HFIPS Director's Fund (Grant No. YZJJ2023QN07), the Anhui Provincial Natural Science Foundation (Grant no. 2008085J19), and the Special Project of Nanhu Laser Laboratory (Grant no. 22-NHLL-ZZKY-005). Finally, a special thanks to Tinney et al for providing the codes for PTGT and LRT algorithms.

References

Alappattu, D. P. and Kunhikrishnan, P. K.: First observations of turbulence parameters in the troposphere over the Bay of Bengal and the Arabian Sea using radiosonde, J. Geophys. Res. Atmos., 115, D06105, 10.1029/2009jd012916, 2010.

Alexander, P., de la Torre, A., Llamedo, P., Hierro, R., Schmidt, T., Haser, A., and Wickert, J.: A method to improve the determination of wave perturbations close to the tropopause by using a digital filter, Atmos. Meas. Tech., 4, 1777-1784, 10.5194/amt-4-1777-2011, 2011.

Anel, J. A., Antuna, J. C., de la Torre, L., Nieto, R., and Gimeno, L.: Global statistics of multiple tropopauses from the IGRA database, Geophys. Res. Lett., 34, 10.1029/2006gl029224, 2007.

Bai, Z., Bian, J., and Chen, H.: Variation in the tropopause transition layer over China through analyzing high vertical resolution radiosonde data, Atmos. Ocean. Sci. Lett., 10, 114-121, 2017.

Bethan, S., Vaughan, G., and Reid, S. J.: A comparison of ozone and thermal tropopause heights and the impact of tropopause definition on quantifying the ozone content of the troposphere, Q. J. R. Meteorol. Soc., 122, 929-944, 10.1002/qj.49712253207, 1996.

Bian, J.: Recent advances in the study of atmospheric vertical structure in upper troposphere and lower stratosphere, Adv. Earth Sci., 24, 262-262, 10.3321/j.issn:1001-8166.2009.03.005, 2009.

Bian, J., Li, D., Bai, Z., Li, Q., Lyu, D., and Zhou, X.: Transport of Asian surface pollutants to the global stratosphere from the Tibetan Plateau region during the Asian summer monsoon, Natl. Sci. Rev., 7, 516-533, 10.1093/nsr/nwaa005, 2020.

Birner, T.: Fine-scale structure of the extratropical tropopause region, J. Geophys. Res. Atmos., 111, D04104, 10.1029/2005jd006301, 2006.

Black, R. X.: Stratospheric forcing of surface climate in the Arctic oscillation, J. Clim., 15, 268-277, 10.1175/1520-0442(2002)015<0268:Sfosci>2.0.Co;2, 2002.

Boothe, A. C. and Homeyer, C. R.: Global large-scale stratosphere-troposphere exchange in modern reanalyses, Atmos. Chem. Phys., 17, 5537-5559, 10.5194/acp-17-5537-2017, 2017.

Butchart, N.: The stratosphere: a review of the dynamics and variability, Weather Clim. Dynam., 3, 1237-1272, 10.5194/wcd-3-1237-2022, 2022.

Chen, H., Bian, J., and Lv, D.: Advances and prospects in the study of stratosphere-tropopause exchange, Chin. J. Atmos. Sci., 30, 813-820, 10.3878/j.issn.1006-9895.2006.05.10, 2006.

Chen, W. and Wei, K.: Anomalous propagation of the quasi-stationary planetary waves in the atmosphere and its roles in the impact of the stratosphere on the East Asian winter climate, Adv. Earth Sci., 24, 272-285, 10.3321j.issn:1001-8166.2009.03.006, 2009.

Christiansen, B.: Downward propagation of zonal mean zonal wind anomalies from the stratosphere to the troposphere: Model and reanalysis, J. Geophys. Res. Atmos., 106, 27307-27322, 10.1029/2000jd000214, 2001.

Danielsen, E. F., Hipskind, R. S., Gaines, S. E., Sachse, G. W., Gregory, G. L., and Hill, G. F.: 3-dimensional analysis of potential vorticity associated with tropopause folds and observed variations of ozone and carbon-monoxied, J. Geophys. Res. Atmos., 92, 2103-2111, 10.1029/JD092iD02p02103, 1987.

De la Torre, A., Tsuda, T., Hajj, G. A., and Wickert, J.: A global distribution of the stratospheric gravity wave activity from GPS occultation profiles with SAC-C and CHAMP, J. Meteorol. Soc. Jpn., 82, 407-417, 10.2151/jmsj.2004.407, 2004.

Feng, S., Fu, Y., and Xiao, Q.: Trends in the global tropopause thickness revealed by radiosondes, Geophys. Res. Lett., 39, 10.1029/2012gl053460, 2012.

Fueglistaler, S., Dessler, A. E., Dunkerton, T. J., Folkins, I., Fu, Q., and Mote, P. W.: Tropical tropopause layer, Rev. Geophys., 47, RG1004, 10.1029/2008rg000267, 2009.

Gamelin, B. L., Carvalho, L. M. V., and Jones, C.: Evaluating the influence of deep convection on tropopause thermodynamics and lower stratospheric water vapor: A RELAMPAGO case study using the WRF model, Atmos. Res., 267, 105986, 10.1016/j.atmosres.2021.105986, 2022.

Gettelman, A. and Forster, P.: A Climatology of the tropical tropopause layer, J. Meteorol. Soc. Jpn., 80, 911-924, 2002a.

Gettelman, A. and Forster, P. M. D.: A climatology of the tropical tropopause layer, J. Meteorol. Soc. Jpn, 80, 911-924, 10.2151/jmsj.80.911, 2002b.

Gettelman, A. and Wang, T.: Structural diagnostics of the tropopause inversion layer and its evolution, J. Geophys. Res. Atmos., 120, 46-62, 10.1002/2014jd021846, 2015.

Gettelman, A., Hoor, P., Pan, L. L., Randel, W. J., Hegglin, M. I., and Birner, T.: The extratropical upper troposphere and lower stratosphere, Rev. Geophys., 49, RG3003, 10.1029/2011rg000355, 2011.

570 Guo, J., Miao, Y., Zhang, Y., Liu, H., Li, Z., Zhang, W., He, J., Lou, M., Yan, Y., Bian, L., and Zhai, P.: The climatology of planetary boundary layer height in China derived from radiosonde and reanalysis data, Atmos. Chem. Phys., 16, 13309-13319, 10.5194/acp-16-13309-2016, 2016.

Han, T., Ping, J., and Zhang, S.: Global features and trends of the tropopause derived from GPS/CHAMP RO data, Sci. China: Phys., Mech. Astron., 54, 365-374, 10.1007/s11433-010-4217-5, 2011.

575 He, S. and Wang, H.: Linkage between the East Asian January temperature extremes and the preceding Arctic Oscillation, Int. J. Climatol., 36, 1026-1032, 10.1002/joc.4399, 2016.

Hersbach, H., Bell, B., Berrisford, P., Hirahara, S., Horanyi, A., Munoz-Sabater, J., Nicolas, J., Peubey, C., Radu, R., Schepers, D., Simmons, A., Soci, C., Abdalla, S., Abellan, X., Balsamo, G., Bechtold, P., Biavati, G., Bidlot, J., Bonavita, M., De Chiara, G., Dahlgren, P., Dee, D., Diamantakis, M., Dragani, R., Flemming, J., Forbes, R., Fuentes, M., Geer, A.,

580 Haimberger, L., Healy, S., Hogan, R. J., Holm, E., Janiskova, M., Keeley, S., Laloyaux, P., Lopez, P., Lupu, C., Radnoti, G., de Rosnay, P., Rozum, I., Vamborg, F., Villaume, S., and Thepaut, J.-N.: The ERA5 global reanalysis, Q. J. R. Meteorol. Soc., 146, 1999-2049, 10.1002/qj.3803, 2020.

Highwood, E. J. and Hoskins, B. J.: The tropical tropopause, Q. J. R. Meteorol. Soc., 124, 1579-1604, 10.1256/smsqj.54910, 1998.

585 Hoerling, M. P., Schaack, T. K., and Lenzen, A. J.: Global objective tropopause analysis, Mon. Weather Rev., 119, 1816-1831, 10.1175/1520-0493(1991)119<1816:Gota>2.0.Co;2, 1991.

Hoffmann, L. and Spang, R.: An assessment of tropopause characteristics of the ERA5 and ERA-Interim meteorological reanalyses, Atmos. Chem. Phys., 22, 4019-4046, 10.5194/acp-22-4019-2022, 2022.

Hoffmann, L., Xue, X., and Alexander, M. J.: A global view of stratospheric gravity wave hotspots located with Atmospheric

590 Infrared Sounder observations, J. Geophys. Res. Atmos., 118, 416-434, 10.1029/2012jd018658, 2013.

Holton, J.: An introduction to dynamic meteorology, Elsevier Academic Press, Burlington, USA2004.

Holton, J. R., Haynes, P. H., McIntyre, M. E., Douglass, A. R., Rood, R. B., and Pfister, L.: Stratosphere-troposphere exchange, Rev. Geophys., 33, 403-439, 10.1029/95rg02097, 1995.

Homeyer, C. R., Bowman, K. P., and Pan, L. L.: Extratropical tropopause transition layer characteristics from high-resolution

595 sounding data, J. Geophys. Res. Atmos., 115, D13108, 10.1029/2009jd013664, 2010.

Homeyer, C. R., Pan, L. L., and Barth, M. C.: Transport from convective overshooting of the extratropical tropopause and the role of large-scale lower stratosphere stability, J. Geophys. Res. Atmos., 119, 2220-2240, 10.1002/2013jd020931, 2014a.

Homeyer, C. R., Pan, L. L., Dorsi, S. W., Avallone, L. M., Weinheimer, A. J., O'Brien, A. S., DiGangi, J. P., Zondlo, M. A., Ryerson, T. B., Diskin, G. S., and Campos, T. L.: Convective transport of water vapor into the lower stratosphere observed

600 during double-tropopause events, J. Geophys. Res. Atmos., 119, 10941-10958, 10.1002/2014jd021485, 2014b.

Huang, R., Chen, W., Wei, K., Wang, L., and Huangfu, J.: Atmospheric dynamics in the stratosphere and its interaction with tropospheric processes: Progress and problems, Chin. J. Atmos. Sci., 42, 463-487, 2018.

Johnston, B. and Xie, F.: Characterizing Extratropical Tropopause Bimodality and its Relationship to the Occurrence of Double Tropopauses Using COSMIC GPS Radio Occultation Observations, Remote Sens., 12, 10.3390/rs12071109, 2020.

Khan, A., Jin, S., and Ieee: Tropopause variations on Tibet from COSMIC GPS Radio Occulation observations, 36th IEEE International Geoscience and Remote Sensing Symposium (IGARSS), Beijing, PEOPLES R CHINA, Jul 10-15, 2016, WOS:000388114603259, 3978-3981, 10.1109/igarss.2016.7730034, 2016.

Kley, D., Stone, E. J., Henderson, W. R., Drummond, J. W., Harrop, W. J., Schmeltekopf, A. L., Thompson, T. L., and Winkler, R. H.: In-situ measurements of the mixing-ratio of water-vapor in the stratosphere, J. Atmos. Sci., 36, 2513-2524, 10.1175/1520-0469(1979)036<2513:Smotmr>2.0.Co;2, 1979.

Koch, S. E., Jamison, B. D., Lu, C. G., Smith, T. L., Tollerud, E. I., Girz, C., Wang, N., Lane, T. P., Shapiro, M. A., Parrish, D. D., and Cooper, O. R.: Turbulence and gravity waves within an upper-level front, J. Atmos. Sci., 62, 3885-3908, 10.1175/jas3574.1, 2005.

Kolstad, E. W., Breiteig, T., and Scaife, A. A.: The association between stratospheric weak polar vortex events and cold air outbreaks in the Northern Hemisphere, Q. J. R. Meteorol. Soc., 136, 886-893, 10.1002/qj.620, 2010.

Kunz, A., Konopka, P., Müller, R., and Pan, L. L.: Dynamical tropopause based on isentropic potential vorticity gradients, J. Geophys. Res. Atmos., 116, https://doi.org/10.1029/2010JD014343, 2011.

Li, D., Vogel, B., Müller, R., Bian, J., Günther, G., Ploeger, F., Li, Q., Zhang, J., Bai, Z., Vömel, H., and Riese, M.: Dehydration and low ozone in the tropopause layer over the Asian monsoon caused by tropical cyclones: Lagrangian transport calculations using ERA-Interim and ERA5 reanalysis data, Atmos. Chem. Phys., 20, 4133-4152, 10.5194/acp-20-4133-2020, 2020.

Li, W., Yuan, Y.-b., Chai, Y.-J., Liou, Y.-A., Ou, J.-k., and Zhong, S.-m.: Characteristics of the global thermal tropopause derived from multiple radio occultation measurements, Atmos. Res., 185, 142-157, 10.1016/j.atmosres.2016.09.013, 2017.

Liang, Z., Rao, J., Guo, D., Lu, Q., and Shi, C.: Northern winter stratospheric polar vortex regimes and their possible influence on the extratropical troposphere, Clim. Dynam., 60, 3167-3186, 10.1007/s00382-022-06494-9, 2023.

Liu, C. and Barnes, E.: Synoptic formation of double tropopauses, J. Geophys. Res. Atmos., 123, 693-707, 10.1002/2017jd027941, 2018.

Liu, Y., Wang, Z., Zhuo, H., and Wu, G.: Two types of summertime heating over Asian large-scale orography and excitation of potential-vorticity forcing II. Sensible heating over Tibetan-Iranian Plateau, Sci. China Earth Sci., 60, 733-744, 10.1007/s11430-016-9016-3, 2017.

Liu, Z., Bai, W., Sun, Y., Xia, J., Tan, G., Cheng, C., Du, Q., Wang, X., Zhao, D., Tian, Y., Meng, X., Liu, C., Cai, Y., and Wang, D.: Comparison of RO tropopause height based on different tropopause determination methods, Atmos. Meas. Tech. Discuss., 2019, 1-19, 10.5194/amt-2019-379, 2019.

Liu, Z., Sun, Y., Bai, W., Xia, J., Tan, G., Cheng, C., Du, Q., Wang, X., Zhao, D., Tian, Y., Meng, X., Liu, C., Cai, Y., and
635   Wang, D.: Comparison of RO tropopause height based on different tropopause determination methods, Adv. Space Res.,
67, 845-857, 10.1016/j.asr.2020.10.023, 2021.

Ma, D., Bian, J., Li, D., Bai, Z., Li, Q., Zhang, J., Wang, H., Zheng, X., Hurst, D. F., and Vomel, H.: Mixing characteristics
within the tropopause transition layer over the Asian summer monsoon region based on ozone and water vapor sounding
data, Atmos. Res., 271, 10.1016/j.atmosres.2022.106093, 2022.

640   Ma, Y., Zhong, L., Jia, L., and Menenti, M.: Land-atmosphere interactions and effects on the climate of the Tibetan Plateau
and surrounding regions, Remote Sens., 15, 286, 10.3390/rs15010286, 2023.

Maddox, E. M. and Mullendore, G. L.: Determination of best tropopause definition for convective transport studies, J. Atmos.
Sci., 75, 3433-3446, 10.1175/jas-d-18-0032.1, 2018.

Meng, L., Liu, J., Tarasick, D. W., Randel, W. J., Steiner, A. K., Wilhelmsen, H., Wang, L., and Haimberger, L.: Continuous
645   rise of the tropopause in the Northern Hemisphere over 1980-2020, Science Advances, 7, 10.1126/sciadv.abi8065, 2021.

Palmen, E.: On the distribution of temperature and wind in the upper westerlies, J. Meterorol., 5, 20-27, 10.1175/1520-
0469(1948)005<0020:Otdota>2.0.Co;2, 1948.

Pan, L. L., Randel, W. J., Gary, B. L., Mahoney, M. J., and Hintsa, E. J.: Definitions and sharpness of the extratropical
tropopause: A trace gas perspective, J. Geophys. Res. Atmos., 109, 10.1029/2004jd004982, 2004.

650   Pan, L. L., Honomichl, S. B., Bui, T. V., Thornberry, T., Rollins, A., Hintsa, E., and Jensen, E. J.: Lapse rate or cold point:
The tropical tropopause identified by in situ trace gas measurements, Geophys. Res. Lett., 45, 10756-10763,
10.1029/2018gl079573, 2018.

Pan, L. L., Paulik, L. C., Honomichl, S. B., Munchak, L. A., Bian, J., Selkirk, H. B., and Voemel, H.: Identification of the
tropical tropopause transition layer using the ozone-water vapor relationship, J. Geophys. Res. Atmos., 119, 3586-3599,
655   10.1002/2013jd020558, 2014.

Park, M., Randel, W. J., Emmons, L. K., and Livesey, N. J.: Transport pathways of carbon monoxide in the Asian summer
monsoon diagnosed from Model of Ozone and Related Tracers (MOZART), J. Geophys. Res. Atmos., 114, D08303,
10.1029/2008jd010621, 2009.

Parracho, A. C., Marques, C. A. F., and Castanheira, J. M.: Where do the air masses between double tropopauses come from?,
660   Atmos. Chem. Phys. Discuss., 2014, 1349-1374, 10.5194/acpd-14-1349-2014, 2014.

Peevey, T. R., Gille, J. C., Homeyer, C. R., and Manney, G. L.: The double tropopause and its dynamical relationship to the
tropopause inversion layer in storm track regions, J. Geophys. Res. Atmos., 119, 10194–10212, 10.1002/2014jd021808,
2014.

Randel, W. and Park, M.: Diagnosing observed stratospheric water vapor relationships to the cold point tropical tropopause, J.
665   Geophys. Res. Atmos., 124, 7018-7033, 10.1029/2019jd030648, 2019.

Randel, W. J. and Park, M.: Deep convective influence on the Asian summer monsoon anticyclone and associated tracer variability observed with Atmospheric Infrared Sounder (AIRS), J. Geophys. Res. Atmos., 111, D12314, 10.1029/2005jd006490, 2006.

Randel, W. J., Seidel, D. J., and Pan, L. L.: Observational characteristics of double tropopauses, J. Geophys. Res. Atmos., 112, D07309, 10.1029/2006jd007904, 2007a.

Randel, W. J., Wu, F., and Forster, P.: The extratropical tropopause inversion layer: Global observations with GPS data, and a radiative forcing mechanism, J. Atmos. Sci., 64, 4489-4496, 10.1175/2007jas2412.1, 2007b.

RavindraBabu, S., Raj, S. T. A., Basha, G., and Ratnam, M. V.: Recent trends in the UTLS temperature and tropical tropopause parameters over tropical South Indian region, J. Atmos. Solar-Terr. Phys., 197, 10.1016/j.jastp.2019.105164, 2020.

Reed, R. J.: A study of a characteristic type of upper-level frontogenesis, J. Meterorol., 12, 226-237, 10.1175/1520-0469(1955)012<0226:Asoact>2.0.Co;2, 1955.

Reichler, T., Dameris, M., and Sausen, R.: Determining the tropopause height from gridded data, Geophys. Res. Lett., 30, 10.1029/2003gl018240, 2003.

Ren, R. C. and Cai, M.: Meridional and vertical out-of-phase relationships of temperature anomalies associated with the Northern Annular Mode variability, Geophys. Res. Lett., 34, 10.1029/2006gl028729, 2007.

Rieckh, T., Scherllin-Pirscher, B., Ladstädter, F., and Foelsche, U.: Characteristics of tropopause parameters as observed with GPS radio occultation, Atmos. Meas. Tech., 7, 3947-3958, 10.5194/amt-7-3947-2014, 2014.

Rosenlof, K. H.: How water enters the stratosphere, Science, 302, 1691-1692, 10.1126/science.1092703, 2003.

Rosenlof, K. H. and Reid, G. C.: Trends in the temperature and water vapor content of the tropical lower stratosphere: Sea surface connection, J. Geophys. Res. Atmos., 113, 10.1029/2007jd009109, 2008.

Santer, B. D., Wehner, M. F., Wigley, T. M. L., Sausen, R., Meehl, G. A., Taylor, K. E., Ammann, C., Arblaster, J., Washington, W. M., Boyle, J. S., and Bruggemann, W.: Contributions of anthropogenic and natural forcing to recent tropopause height changes, Science, 301, 479-483, 10.1126/science.1084123, 2003a.

Santer, B. D., Sausen, R., Wigley, T. M. L., Boyle, J. S., AchutaRao, K., Doutriaux, C., Hansen, J. E., Meehl, G. A., Roeckner, E., Ruedy, R., Schmidt, G., and Taylor, K. E.: Behavior of tropopause height and atmospheric temperature in models, reanalyses, and observations: Decadal changes, J. Geophys. Res. Atmos., 108, 10.1029/2002jd002258, 2003b.

Sausen, R. and Santer, B. D.: Use of changes in tropopause height to detect human influences on climate, Meteorol. Z., 12, 131-136, 10.1127/0941-2948/2003/0012-0131, 2003.

Schmidt, T., Wickert, J., Beyerle, G., and Reigber, C.: Tropical tropopause parameters derived from GPS radio occultation measurements with CHAMP, J. Geophys. Res. Atmos., 109, D13105, 10.1029/2004jd004566, 2004.

Schmidt, T., Beyerle, G., Heise, S., Wickert, J., and Rothacher, M.: A climatology of multiple tropopauses derived from GPS radio occultations with CHAMP and SAC-C, Geophys. Res. Lett., 33, 10.1029/2005gl024600, 2006.

Seidel, D. J. and Randel, W. J.: Variability and trends in the global tropopause estimated from radiosonde data, J. Geophys. Res. Atmos., 111, 10.1029/2006jd007363, 2006.

700   Seidel, D. J., Ross, R. J., Angell, J. K., and Reid, G. C.: Climatological characteristics of the tropical tropopause as revealed by radiosondes, J. Geophys. Res. Atmos., 106, 7857-7878, 10.1029/2000jd900837, 2001.

Shangguan, M., Wang, W., and Jin, S.: Variability of temperature and ozone in the upper troposphere and lower stratosphere from multi-satellite observations and reanalysis data, Atmos. Chem. Phys., 19, 6659-6679, 10.5194/acp-19-6659-2019, 2019.

Shepherd, T. G.: Issues in stratosphere-troposphere coupling, J. Meteorol. Soc. Jpn., 80, 769-792, 10.2151/jmsj.80.769, 2002.

705   Sun, N., Fu, Y., Zhong, L., Zhao, C., and Li, R.: The impact of convective overshooting on the thermal structure over the Tibetan Plateau in summer based on TRMM, COSMIC, Radiosonde, and Reanalysis Data, J. Clim., 34, 8047-8063, 10.1175/jcli-d-20-0849.1, 2021.

Tang, C., Li, X., Li, J., Dai, C., Deng, L., and Wei, H.: Distribution and trends of the cold-point tropopause over China from 1979 to 2014 based on radiosonde dataset, Atmos. Res., 193, 1-9, 10.1016/j.atmosres.2017.04.008, 2017.

710   Thompson, A. M., Stauffer, R. M., Wargan, K., Witte, J. C., Kollonige, D. E., and Ziemke, J. R.: Regional and seasonal trends in tropical ozone From SHADOZ profiles: Reference for models and satellite products, J. Geophys. Res. Atmos., 126, 10.1029/2021jd034691, 2021.

Thuburn, J. and Craig, G. C.: On the temperature structure of the tropical substratosphere, J. Geophys. Res., 107, ACL10-11-10, 2002.

715   Tian, H., Tian, W., Luo, J., Zhang, J., and Zhang, M.: Climatology of cross-tropopause mass exchange over the Tibetan Plateau and its surroundings, Int. J. Climatol., 37, 3999-4014, 10.1002/joc.4970, 2017.

Tinney, E. N., Homeyer, C. R., Elizalde, L., Hurst, D. F., Thompson, A. M., Stauffer, R. M., Vomel, H., and Selkirk, H. B.: A modern approach to a stability-based definition of the tropopause, Mon. Weather Rev., 150, 3151-3174, 10.1175/mwr-d-22-0174.1, 2022.

720   Tomassini, L., Gerber, E. P., Baldwin, M. P., Bunzel, F., and Giorgetta, M.: The role of stratosphere-troposphere coupling in the occurrence of extreme winter cold spells over northern Europe, J. Adv. Model. Earth Sy., 4, 10.1029/2012ms000177, 2012.

Wang, W., Matthes, K., Schmidt, T., and Neef, L.: Recent variability of the tropical tropopause inversion layer, Geophys. Res. Lett., 40, 6308-6313, 10.1002/2013gl058350, 2013.

725   Wirth, V.: Thermal versus dynamical tropopause in upper-tropospheric balanced flow anomalies, Q. J. R. Meteorol. Soc., 126, 299-317, 10.1256/smsqj.56214, 2000.

WMO: Meteorology: A three-dimensional science: second session of the commission for aerology, WMO Bulletin, 4, 134–138, 1957.

Woo, S.-H., Kim, B.-M., and Kug, J.-S.: Temperature variation over East Asia during the lifecycle of weak stratospheric polar

730   vortex, J. Clim., 28, 5857-5872, 10.1175/jcli-d-14-00790.1, 2015.

Wu, G., Zhuo, H., Wang, Z., and Liu, Y.: Two types of summertime heating over the Asian large-scale orography and excitation of potential-vorticity forcing I. Over Tibetan Plateau, Sci. China Earth Sci., 59, 1996-2008, 10.1007/s11430-016-5328-2, 2016.

Xia, P., Shan, Y., Ye, S., and Jiang, W.: Identification of tropopause height with atmospheric refractivity, J. Atmos. Sci., 78, 3-16, 10.1175/jas-d-20-0009.1, 2021.

Xian, T. and Fu, Y.: Characteristics of tropopause-penetrating convection determined by TRMM and COSMIC GPS radio occultationmeasurements, J. Geophys. Res. Atmos, 120, 7006-7024, 10.1002/2014JD022633, 2015.

Xian, T. and Fu, Y.: A hiatus in the tropopause layer change, Int. J. Climatol., 37, 4972-4980, 10.1002/joc.5130, 2017.

Xian, T. and Homeyer, C. R.: Global tropopause altitudes in radiosondes and reanalyses, Atmos. Chem. Phys., 19, 5661-5678, 10.5194/acp-19-5661-2019, 2019.

Xie, F., Tian, W., Zhou, X., Zhang, J., Xia, Y., and Lu, J.: Increase in lower stratospheric water vapor in the past 100 years related to tropical Atlantic Warming, Geophys. Res. Lett., 47, e2020GL090539, 10.1029/2020gl090539, 2020.

Xu, X., Gao, P., and Zhang, X.: Global multiple tropopause features derived from COSMIC radio occultation data during 2007 to 2012, J. Geophys. Res. Atmos., 119, 8515-8534, 10.1002/2014jd021620, 2014.

Xu, X., Dong, L., Zhao, Y., and Wang, Y.: Effect of the Asian Water Tower over the Qinghai-Tibet Plateau and the characteristics of atmospheric water circulation, Chin. Sci. Bull., 64, 2830-2841, 2019.

Yang, J. and Lv, D.: Simulation of Stratosphere-Troposphere Exchange Effecting on the Distribution of Ozone over Eastern Asia, Chin. J. Atmos. Sci., 28, 579-588, 10.1117/12.528072, 2004.

Zeng, X., Xue, X., Dou, X., Liang, C., and Jia, M.: COSMIC GPS observations of topographic gravity waves in the stratosphere around the Tibetan Plateau, Sci. China Earth Sci., 60, 188-197, 10.1007/s11430-016-0065-6, 2017.

Zhang, J., Tian, W., Chipperfield, M. P., Xie, F., and Huang, J.: Persistent shift of the Arctic polar vortex towards the Eurasian continent in recent decades, Nat. Clim. Change, 6, 1094-1099, 10.1038/nclimate3136, 2016.

Zhang, Y., Si, D., Ding, Y., Jiang, D., Li, Q., and Wang, G.: Influence of major stratospheric sudden warming on the unprecedented cold wave in East Asia in January 2021, Adv. Atmos. Sci., 39, 576-590, 10.1007/s00376-022-1318-9, 2022.

Zhang, Y.-X., Si, D., Liu, Y.-J., Mei, M., and Wang, G.-F.: Stratosphere-troposphere synergetic effect on the extreme low-temperature event over China in late November 2022, Adv. Clim. Change Res., 14, 671-680, 10.1016/j.accre.2023.09.014, 2023.

Zhuo, W., Yao, Y., Luo, D., Simmonds, I., and Huang, F.: Combined impact of the cold vortex and atmospheric blocking on cold outbreaks over East Asia and the potential for short-range prediction of such occurrences, Environ. Res. Lett., 17, 10.1088/1748-9326/ac8362, 2022.